



Swansea University
Prifysgol Abertawe



Cronfa - Swansea University Open Access Repository

This is an author produced version of a paper published in :

Acta Materialia

Cronfa URL for this paper:

<http://cronfa.swan.ac.uk/Record/cronfa29194>

Paper:

Birosca, S. (2016). The Hierarchy of Microstructure Parameters Affecting the Tensile Ductility in Centrifugally Cast and Forged Ti-834 Alloy during High Temperature Exposure in Air. *Acta Materialia*

<http://dx.doi.org/10.1016/j.actamat.2016.07.015>

This article is brought to you by Swansea University. Any person downloading material is agreeing to abide by the terms of the repository licence. Authors are personally responsible for adhering to publisher restrictions or conditions. When uploading content they are required to comply with their publisher agreement and the SHERPA RoMEO database to judge whether or not it is copyright safe to add this version of the paper to this repository.

<http://www.swansea.ac.uk/iss/researchsupport/cronfa-support/>

The Hierarchy of Microstructure Parameters Affecting the Tensile Ductility in Centrifugally Cast and Forged Ti-834 Alloy during High Temperature Exposure in Air

P. Davies¹, R. Pederson², M. Coleman¹, S. Biroasca¹

¹ Institute of Structural Materials, College of Engineering, Swansea University, Bay Campus, Fabian Way, Swansea SA1 8EN, United Kingdom.

² Research and Technology Centre, GKN Aerospace Engine Systems Sweden, SE-46181 Trollhättan, Sweden.

Abstract

Ductility regression is the main concern in using Ti-834 titanium alloy at temperatures above 500°C for aerospace applications. The reduction of ductility in titanium alloys at high temperatures is strongly correlated to the exposure time. In the current study the effect of prolonged exposure at 500°C on the tensile ductility of two differently processed Ti-834 alloys was investigated. In order to simulate actual Ti-834 processing routes, forged and centrifugally cast materials were used. The tensile tests were conducted on various specimens exposed at 500°C for 100, 200 and 500 hours to observe microstructure feature changes. Moreover, the effect of microstructure, microtexture, α -case, α_2 and silicide precipitate coarsening during high temperature exposure was studied thoroughly. The cast alloy was found to have a minimum ductility and failed at 1.8% strain after exposure at 500°C/500 hour when the α -case layer was retained during testing, whilst, the ductility of the forged alloy was unaffected. The effects of individual microstructural parameters on the ductility regression in Ti-834 alloy were quantified. The results showed that 7.1% strain differences between the cast and forged alloy are related to microstructural variations including; morphology, lath widths, grain size and shape, grain orientations and microtexture. A total of 9.6 % strain loss

was observed in centrifugally cast Ti-834 after aging at 500°C/500h and quantified as follow; 3.6% due to α -case formation during high temperature exposure, 0.2% due to α_2 -precipitates coarsening, 4.4% due to further silicide formation and coarsening, 1.4% due to additional microstructure changes during high temperature exposure. Furthermore, silicide coarsening on α/β phase boundaries caused large void formation around the precipitates. A theoretical model supported by experimental observations for silicide precipitation in fully colony and duplex microstructures was established. The element partitioning during exposure caused Al and Ti depletion in the vicinity of the β phase in the lamellae, *i.e.*, α_s area. This resulted in lowering the strength of the alloy and facilitated the formation of $Ti_3(SiZr)_2$ precipitates. The Al depletion and nano-scale partitioning observed at the α_s/β boundaries resulted in easy crack initiation and promoted propagation in the centrifugally cast colony microstructure and reduced the basal slip τ_{crss} . Furthermore, silicides were not formed in α_p (high Al, Ti and low Zr areas) in the forged duplex microstructure that promoted superior mechanical performance and ductility over the cast alloy.

Keywords: Ti-834 Alloy, Ductility, Microstructure, Silicide, Alpha Case.

1. Introduction

Near alpha titanium alloys such as Ti-6242S and Ti-834 are extensively used for intermediate to high temperature applications in the gas turbine. These types of high temperature alloys are selected due to their balance of strength, fatigue and creep properties. The near alpha titanium alloys are designed to have low volume fractions of beta phase (β), which is achieved through limiting the amount of β stabilizing elements with increasing alpha (α) stabilizing elements [1]. In general, silicon is also added to near alpha titanium alloys to improve their creep resistance and strength at elevated temperatures. Titanium alloys exposed to high temperatures (above 500°C) for extended periods are known to experience a reduction in mechanical properties; including a loss of ductility

[2], a reduction in fatigue performance [3] and reduced creep resistance [4]. It is reported that the reduction in fatigue life [5] [6] and creep resistance [4] can largely be attributed to the formation of an oxygen rich phase at the surface. This hard and brittle oxygen rich layer; commonly known as α -case [7] forms simultaneously with an oxide scale (TiO_2) at the surface during prolonged exposure at temperatures in excess of 480°C [8]. Inward diffusion of oxygen proceeds through this oxide scale due to the high affinity of titanium to absorb oxygen. This stabilizes the α phase resulting in a region below the surface free of β phase [7], [9]. The loss of ductility is not well understood and cannot solely be correlated to α -case formation. Other studies [2] [10] have attributed the loss in ductility to the precipitation of coherent Ti_3Al , *i.e.*, α_2 particles in conjunction with the formation of silicides. It is believed that the precipitation of coherent α_2 particles is encouraged by the presence of tin, resulting in higher volume fractions of α_2 precipitates in titanium alloys [1]. It is also reported that the α_2 particles become effective obstacles to dislocation creep [1], [2], [10]. In general, using near alpha titanium alloys above α_2 solvus temperature is not recommended, especially where creep resistance is required. It should be noted that the solvus temperature of the α_2 precipitates is composition dependent, thus in Ti-6242S is $\sim 650^\circ\text{C}$ while in Ti-834 it is $\sim 750^\circ\text{C}$ [11]. Silicon on the other hand is usually present in solid solution following final processing. However as reported in [2],[10],[12] the transformation of β phase during cooling can result in α_2 and fine silicide particles formation in titanium alloys. It should be emphasised here, that silicide solvus temperatures are much higher than the α_2 phase and have been determined for Ti-6242S and Ti-834 to be $\sim 945^\circ\text{C}$ and 990°C , respectively [10],[12].

Since its introduction in the 1980's, the microstructurally optimised near α Ti-834 alloy has been mainly utilised for elevated temperature applications in the gas turbine. Initially, the Ti-834 alloy was developed as a wrought alloy [13], having a microstructure consisting of primary alpha (α_p) in addition to a transformed β structure, used in rotating structural applications [14]. It was originally designed to maximize creep and low cycle fatigue performance up to temperatures of approximately

600°C. This was achieved through a combination of alloying and heat treatments in addition to microstructure optimisation. It is reported that maximum ductility for the alloy in the forged condition was found to correspond with a volume fraction of ~20% α_p , which delivers satisfactory creep and fracture toughness performance and providing good crack propagation resistance [12]. Recently, Ti-834 alloy is being reconsidered for use in cast form for static structural applications. In contrast to the wrought material, the cast form of Ti-834 exhibits a colony β -transformed microstructure [15]. This variation in microstructure results in a different balance of mechanical properties to the forged material. It was shown that the strength of cast Ti-834 at room and elevated temperatures were comparable to the wrought material, and the cast alloy provided better creep resistance than its wrought equivalent [14]. However, the same study reported that the cast alloy showed less ductility, especially at room temperature, compared to the forged material. Furthermore, the low cycle fatigue performance of the cast alloy was also found to be inferior to that of the wrought form of the alloy [11].

Environmental legislation and the desire to reduce operating costs have resulted in a sustained drive from manufacturers to improve aero engine efficiency and reduce emissions [16], [17]. This can be achieved via increased engine operating temperatures, which reduce both greenhouse gas emissions and fuel consumption. For higher combustion and turbine entry temperatures to become a reality, temperatures must be increased in the intermediate compressor region of the engine. With current compressor operating temperatures of up to 450°C, Ti 6242S is currently the preferred alloy for manufacturing compressor casings. However it is desirable to increase thermodynamic efficiency, to increase operating temperatures towards 500°C in the intermediate compressor section. As a result Ti 6242S will need to be replaced with an alternative alloy with higher operating temperature capabilities. The impracticalities and excessive cost implications of manufacturing casings exclusively from forged material is a major issue. Therefore, an alternative to the Ti-6242S alloy in a cast form is a more desirable choice for intermediate compressor casings in the wake of increasing

demand of cost effective hotter engine. Ductility is a key property for intermediate compressor casings, which are required to absorb high energies in the event of an engine failure; therefore in the current study the effect of long time exposure at 500°C on ductility regression of centrifugally cast Ti-834 was investigated.

In general, the forged material in the intermediate compressor casing is found in the form of rolled rings. The initial forging procedure consists of an upset forging operation where billet undergoes large reductions that are typically performed above the β transus to avoid cracking. The billet is then pierced through the center to create a cylinder. Further work in the $\alpha+\beta$ field is then applied to the material in the form of two rings that apply a uniform pressure and turn the cylinder. The internal diameter of the cylinder increases while its thickness is reduced until the final shape of the ring is achieved [1], [7], [11], [13]. However, in the wake of recent developments in centrifugal casting, the demand to replace forged materials with the cast form of the alloy has increased. Centrifugal casting utilizes centrifugal forces that are created when the mold is rotated around its axis at high speed (300 to 3000 rpm). Molten metal is forced to the mold wall where it freezes in order to form the desired shape. Hot Isostatic Pressing (HIP) is used to eliminate any internal porosity after casting [18]. Therefore, the current study is mainly focused on comparing detailed microstructure and mechanical property differences between the forged and centrifugal cast Ti-834 alloys. Furthermore, the effect on α -case, microstructure including α_2 and silicide volume fractions and distributions; α and β morphology on ductility during tension were investigated. The Ti-834 alloy was exposed to various times at 500°C in order to observe the microstructure changes and corresponding mechanical property in cast and forged alloys.

2. Experimental Procedures

The chemical composition of the Ti-834 used in this study was: Ti 5.8 Al - 4.0 Sn - 3.5 Zr - 0.7 Nb - 0.5 Mo - 0.35 Si wt %. Billets from the same population were used as feedstock for both the forged and cast material. The centrifugal cast samples was produced and supplied by Doncaster Settas/UK in the form of 25mm diameter cast bars. The centrifugal cast Ti-834 test bars were HIP'd (Hot Isostatic Pressing) at 965°C under 100MPa for 2h; then vacuum heat treated at 965°C/1h, Ar gas fan cool to 150°C; then aged at 621°C/2h, Ar gas fan cool to 150°C. The forged alloy was produced and supplied by Forgital Group S. P. A./Italy, in the form of sections of forged rings. After forging, the rings were hot expanded to final size by Forgital Italy. Sections of the forged rings were heat treated by TIMET UK: solution treatment at 1025°C/1h, AC, then aged 621°C/2h, AC.

Cylindrical tensile specimens were prepared with the geometry shown in Figure 1a. A number of both centrifugally cast and forged specimens were then exposed to an elevated temperature of 500°C for 100, 200 and 500 h followed by Air Cooling (AC) to determine the effect different exposure times had on the monotonic performance. Further procedures were conducted in order to identify the effects of α -case, α_2 particles and silicides separately on the tensile ductility. First, in order to understand the exact influence of α -case on the alloys ductility, tensile tests were performed on the specimens with the resulting α -case retained, followed by tensile testing specimens with the α -case removed. This is conducted through initially machining samples with the diameter of 0.5 mm oversize and subsequently machining to the correct diameter; removing the α -case accordingly. Further heat treatments were conducted on the centrifugally cast alloy to gain a better understanding of the effects of silicide and α_2 precipitates on tensile ductility of Ti-834. A number of the originally exposed (500°C/500h) oversized specimens were subjected to further heat treatments at 800°C/2h AC and 1000°C/2h AC in order to dissolve the α_2 precipitates and silicides present in the alloy, respectively. Following the heat treatments, standard tensile tests were performed. All tensile tests were conducted using a Schenck electric screw machine utilising a Dartec 9610 control system. Tensile tests were performed at room temperature in accordance with

BS EN 2002-1:2005 utilising a side-mounted extensometer with a gauge length of 25mm. A dual strain rate was employed with a strain ramp shortly after yield point during the tensile test. This is a typical industrial testing practise, which is mainly because most of the fracture in aerospace component occurred in high strain rate rather than in low strain rate, however, in order to obtain reliable data in elastic region a lower strain rate is used before yielding. In general titanium alloys show strain rate sensitivity during loading. For instance, Ti-834 alloy showed that both yield strength and UTS increased, while total elongation decreased in line with higher strain rates [19]. Therefore it would be reasonable to expect that the UTS and elongation recorded during this investigation could be affected similarly to the findings in [19]. Nonetheless, the same strain rate and strain ramp are used for both cast and forged alloys during tensile tests, therefore, any effect of strain ramp that might have on ductility would be the same on both alloys. Moreover, in the current study, the results are reported in strain (%) as the authors believe this provides a more accurate measurement of tensile ductility when compared to elongation over 4D. Errors can be introduced when using 4D method as the fractured specimens are required to be re-joined in order to measure elongation. The 4D elongation method measures the percentage elongation over a gauge length of 4D; where 4D equates to 4 times the diameter of the specimen gauge length.

The microstructure and microtexture characterisation of as-received and post failed specimens were carried out for both forged and centrifugally cast Ti-834 samples using optical and Scanning Electron Microscope (SEM) in addition to Electron Backscatter Diffraction (EBSD) and Energy Dispersive Spectroscopy (EDS). To aid in metallographic analysis, the specimens were mounted in conductive Bakelite prior to a series of grinding and polishing steps culminating in a final polish performed with a Beuhler VibroMet 2 vibration polisher, using a non-crystallising colloidal silica solution (0.04 μm) for 15 to 60 minutes. The final step carried out in the metallographic preparation was to etch the surface of the material to enable the microstructure to be viewed through an Optical Microscope (OM). Kroll's Reagent with a composition of 1-2% HF, 8-9% HNO₃ and remainder

H₂O was used for this purpose. The etching process involved submerging the surface of the alloy in the etchant for ~ 25 seconds. Subsequently, the specimens were thoroughly rinsed under running water. A Reichart MeF3 microscope in conjunction with Nikon Imaging Software was then used to observe the microstructure and α -case on both forged and cast processed alloys. The average grain size of the cast alloy was determined using the Mean Linear Intercept (M.L.I.) method. A variation of the M.L.I. method was used to calculate the average α_p grain size of the cast alloy. This method takes into account the volume fraction of α_p grains ($V_{V,\alpha}$) via Equation 1.

$$M. L. I. = \frac{V_{V,\alpha} L_T}{N_\alpha} \dots\dots\dots (1)$$

Where L_T and N_α equal the total test line length and number of α_p grains, respectively. Following OM and SEM observations, the EBSD data were collected using a Nordlys EBSD detector and HKL Technology Channel 5 EBSD system interfaced to a Phillips FEI XL30 SEM. The SEM operating voltage used was 20 kV to optimise the quality of the diffraction patterns. The analysis was conducted using standard HKL-EBSD Channel 5 software package. Furthermore, high-resolution imaging and EDS analysis were performed on a JOEL 7800 FEG-SEM equipped with AZTEC data acquisition and analysis software. The forged and ring rolled alloys were received from Forgital Group in cylindrical shapes. The EBSD scans area of the forged alloy is shown in Figure 1b. For comparison purposes the testing loading direction aligned with forged and casting directions. In order to obtain a 3D EBSD map from the Area of Interest (AOI), subsequent EBSD scans were performed at 10, 50, 100 and 200 μm below the sample surface by removing material using conventional grinding and polishing technique. This quasi-3D construction of an EBSD map was necessary to identify the crystallographic information from individual maps as well as the crack initiation location and propagation path in 3D.

3. Results and Discussion

3.1 Microstructure Investigation of the Original and Exposed Materials

The as-received microstructures of centrifugally cast and forged Ti-834 alloys are shown in Figures 2a and 2b, respectively. It is evident from the figures that the cast and forged materials display vastly different microstructures; exhibiting fully lamellar (widmanstatten) and duplex microstructures, respectively. The cast microstructure exhibits an equiaxed prior β grain structure with an average size of approximately $850\mu\text{m}$ in diameter. The β grains are surrounded by a continuous layer of Grain Boundary α (GB_α) several microns in width. As shown in Figure 2a, each prior β grain typically contains a few α colonies produced from a large number of individual aligned α lamellae with an average width of $\sim 4\mu\text{m}$. Whilst, the wrought, *i.e.*, forged microstructure exhibits a homogenous duplex microstructure with equiaxed α_p grains distributed in a transformed β matrix, see Figure 2b. The transformed regions contain a combination of aligned α colony and basketweave morphology within the β matrix. Furthermore, the wrought material was found to consist of $\sim 36\%$ α_p volume fraction with an average α_p grain size of approximately $20 \pm 3 \mu\text{m}$.

As shown in Figures 2b and 2d, the exposure of Ti-834 at the elevated temperature of 500°C had no significant effects on the microstructure of forged material. The exposure temperature was well below β -transus temperature, therefore, the slight variation of the average prior β grain size of the cast alloy following exposure may be related to microstructure heterogeneity of the processed alloys. Moreover, a slight change of $1 \pm 0.4 \mu\text{m}$ in the GB_α width and $1 \pm 0.7 \mu\text{m}$ in α lath width were observed in the centrifugally cast alloy, see Figures 2a and 2c. Similar observations were found in the forged alloy, where an increase of $\sim 0.8\%$ in α_p volume fraction was recorded and the average α_p grain size remained similar; within $\pm 0.9 \mu\text{m}$ range variation.

3.2 The Effects of Microstructure on the overall Ductility in Ti-834 Alloy

As shown in Figures 3 and 4, the forged material in the unexposed and exposed for 100, 200 and 500 h conditions is stronger and more ductile than its centrifugally cast equivalent. The table shown in Figures 3 and 4 show UTS (MPa), 0.2% Proof Stress (MPa), Modulus (GPa) and strain (%) values, generated during each tensile test. It is clear from the figures that the forged material in the unexposed condition has a significantly higher tensile strength with both the UTS and 0.2% proof stress values being approximately 10% higher than those recorded for the centrifugally cast material. Ductility was also far greater in the forged material; with a failure strain of 18.4% compared to 11.3% for the cast material. It was also evident that exposure at 500°C has a dramatic effect on the tensile ductility of the cast material. As shown in Figure 3, the ductility was reduced to 1.8% from 11.3% after 500 hours exposure; intermediate values of 6.2% and 5.1% were recorded after 100 and 200 hours exposure, respectively. Moreover, the low UTS value recorded after 500 hours exposure is a result of the premature fracture limiting the tensile strength. However, slight increases are seen in 0.2% proof stress and modulus as exposure times increase. Unlike the Ti-834 cast material no loss of ductility was recorded in line with increasing exposure times for the forged alloy, see Figure 4. However, as occurred with the cast alloy a similar variability for 0.2% proof stress and modulus values were also observed in forged alloy.

It is clear from Figures 3 and 4, that the forged Ti-834 alloy displayed better monotonic properties than the centrifugally cast alloy in the unexposed condition. The microstructure differences between the two processed alloys shown in Figure 2 play a vital role in the plastic deformation and failure mechanisms. It was evident from Figures 2b and 2d that the duplex microstructure in the forged material has a small equiaxed α_p grain size and a narrow width of the lamellae (α_s) within the transformed β matrix. This provides very short effective slip lengths within the α phase and crack retardation at α_p /transformed β boundaries. In contrast the colony microstructure for the cast alloy

shown in Figure 2a and 2c provides long effective slip lengths. Previous studies [20], [21] on Ti-6Al-4V have shown that the misorientation angles between α lamellae in titanium alloys can be extremely small. This was also found to be the case in the cast Ti-834 alloy shown in the EBSD orientation map in Figure 5, where a large number of α lamellar within each colony have very similar orientations, resulting in very low angle grain boundaries between them. The misorientation angles are shown for L1 (Line 1) and L2 (Line 2) in the same figure. It is clear that the average misorientation angle between the α lamellae is 0.6° in L1 and 0.9° in L2. This results in far longer effective slip lengths in the cast alloy ($\sim 450 \mu\text{m}$) than those in the forged alloy ($\sim 20 \mu\text{m}$) using statistical average assumption. Thus, crack propagation within the colony microstructure, *i.e.*, cast alloy, is much faster than in the duplex microstructure, *i.e.*, forged alloy. The colony morphology provides an easy crack path through each colony with no deviation; only arresting when they encounter prior β grain boundaries or other α colonies with vastly different orientations. This is in agreement with findings in previous studies [20] [21] [22]. Hall, [22] stated that a fine microstructure with short distances between interfaces, small grains and without a preferred crystallographic macro- or microtexture is desired for resistance to crack nucleation and early growth in Ti alloys. As shown in Figures 3 and 4, the microstructure parameter contributed 7.1% to the ductility reduction at RT test conditions. As can be seen from the same figures, 18.5% ductility was observed in the forged alloy, whilst only 11.4% was recorded for cast alloy. This indicates that the microstructure and morphology would also have an influence on ductility at high temperature testing as will be discussed in the next sections. It is clear from the current study that microstructure is strongly correlated with the mechanical properties of the alloys hence, strength and ductility.

A 3D-EBSD technique was employed in order to determine exact crack initiation location in the cast alloy and observe the crack path within the bulk sample. As described earlier, the EBSD scans were carried out around the crack on the Loading Direction – Transverse Direction (LD-TD) plane at the surface (removing $10\mu\text{m}$ for surface preparation purposes) of the tested sample as well as 50,

100 and 200 μm below the sample (LD-TD) surface, see Figure 6a, 6b and 6c, respectively. The amount of material removed between each EBSD scan was guided by the optical and scanning electron microscopes. The aim was to find the original point where the crack initiated by polishing further down from LD-TD surface along Normal Direction (ND) to the images shown in Figure 6, until the crack initiation point was reached. Figure 6a-c shows Inverse Pole Figure (IPF)s // LD with schematic 3D hexagons added to some lamellae/colonies along the crack path for better visualisation of the crystallographic orientation of these critical α lamellae. Five areas are indicated on the IPF maps by white dashed rectangular lines and are magnified individually to reveal more detail in the figures. Figures 6a.1, 6b.1 and 6c.1 represent $\langle a \rangle$ basal slip, *i.e.*, (0002) $\langle 11\text{-}20 \rangle$ Schmid factor maps for the maps in 6a-c, with the stress axis in the horizontal direction of the images (LD // X-axis). Whilst, Figures 6a.2, 6b.2 and 6c.2 represent $\langle a \rangle$ prismatic slip, *i.e.*, (10-10) $\langle 11\text{-}20 \rangle$ Schmid factor maps for the same IPF maps in 6a-c. It is clear from Figures 6c, 6c.1 and 6c.2 that the crack was initiated at a prior β grain triple junction, where three prior β grains with different crystallographic orientations met. This indicates that prior β grain size and orientation have direct effect of crack initiation and propagation. It is reported in [20], [21] that the prior β triple junction was responsible for crack bifurcation in Ti alloys during low cycle fatigue tests, however, in the current study it appears that is also a favourable location for crack initiation during tensile tests.

It is evident from Figure 6 that the majority of the crack propagation is of trans-lamellar nature with only a few segments of the crack having grown parallel to the lamellar interface (referred to as inter-lamellar). Looking at the five magnified areas in Figure 6 it is evident that in most cases the crack encounter the lamellar colonies at a 90° angle to one in-plane direction of the α lamellae interface. It is also clear from the Schmid factor maps that the crack easily crossed the lamellae favourably oriented for $\langle a \rangle$ basal slip while lamellae with a high Schmid factor for $\langle a \rangle$ prismatic slip tended to deviate or impede crack propagation. The crack arrest is clearly visible on prior β

boundaries (Figure 6a-c: areas 3, 4 and 5) or within (Figure 6a-c: area 1, 2 and 5) lamellae favourably oriented for prismatic $\langle a \rangle$ slip system activation. In the present study, statistical Schmid factor analysis of the EBSD maps showed that about 20% of the crack length displayed inter-lamellar crack growth, and had grains favourably orientated for prismatic slip, whilst 80% were more likely to undergo basal slip and displayed trans-lamellar crack growth.

It is generally believed that the crystallographic texture has a great influence on mechanical property, hence on deformation mechanism in titanium alloys [20-23]. Thus, in order to obtain statistically reliable texture measurement large EBSD mappings (5×5 mm) performed on both cast and forged alloys. It is clear from Figures 7a and 7b that the cast Ti-834 alloy has relatively stronger texture intensity than the forged alloy; 11.2 and 4.7 times above random texture, respectively. Moreover, it appears that the two alloys have very different textures. From the IPFs, PFs and ODFs in Figure 7a, it is evidence that the strongest texture component in the cast alloy is 30° away from typical deformation Basal texture component (0001) $\langle 10-10 \rangle$. The cast alloy also has a weak texture intensity of Transverse texture component (10-10) $\langle 0001 \rangle$, see Figure 7c for schematic representation of typical texture components in Ti alloys. It is generally believed that $25-35^\circ$ away from (0001) indicates on recrystallisation occurrence during processing [24]. The appearance of recrystallisation texture components in the cast alloy is expected, as dynamic and static recrystallisations are likely to occur during casting and following heat treatment, respectively. From Figure 7b, it seems that the strongest texture component in the forged alloy is 8° away from typical deformation texture component of (11-20) $\langle 0001 \rangle$ with weak shear texture components. Furthermore, the forged alloy has also a relatively weak 5° away from $\langle 0001 \rangle$ – Fibre and relatively strong $\langle 10-10 \rangle$ – Fibre textures which indicate on severe deformation during processing. This is also expected, as shear deformation is prone to occur during heavy deformation such as ring rolling and forging. The shear deformation occurred during forging, may have weakened the overall texture intensity of forged alloy compared to the cast alloy. Overall, the high texture intensity in the

cast alloy with strong near Basal texture component has accelerated an easy activation of (0002) $\langle 11\text{-}20 \rangle$ slip system in the vast majority of the lamellae within individual colonies as shown in Figures 6a₁, 6b₁ and 6c₁. It appears that this strong texture is greatly assisted in easy crack propagation through the lamellae in the colony microstructure, and hence contributed in ductility reduction.

It seems that the microstructure and overall texture differences between the cast and forged alloys have a great effect on crack initiation and propagation. It is well established that a columnar lamellar microstructure can provide long unrestricted slip paths [22], [23], resulting in poor low cycle fatigue resistance compared to a lamellar microstructure with a basket-weave morphology which provide a more tortuous crack path and lower growth rate [25], [26]. It is evident from the current study that this approach is also true for crack path in Ti-834 during tensile testing. The presence of basket-weave morphology within transformed β matrix in the duplex forged microstructure has assisted in crack retardation and diversion greatly. This is because the lamellae in basket-weave microstructure have more random orientation than the lamellae in the fully colony microstructure where there is no crack diversion or retardation observed in large numbers of lamellae which provided unrestricted slip path, see Figure 6. It is well established that equiaxed α_p showed easy activation of prismatic $\langle a \rangle$ slip in comparison to easy basal $\langle a \rangle$ slip in α_s lamellae in Ti-alloys [24], which is more related to Al content, as will be discussed in Section 3.5. This may also have assisted in better crack propagation resistance in the forged duplex microstructure.

3.3 The α -Case effects on Overall Ductility in Ti-834 Alloy

As illustrated in Figures 8a and 8b both the centrifugally cast and forged materials had developed a relatively uniform α -case layer (5-7 μm in depth) after 500 h exposure at 500°C. This brittle α -case layer can be easily cracked during loading; resulting in a large number of cracks developing at the

surface of the exposed cast and forged specimens as shown in Figure 8. It is evident from Figures 8c and 8d, that the extended cracks from α -case to the bulk material in the centrifugally cast alloy were much longer than seen in forged Ti-834 alloy. As shown in the Figure 8c, the crack easily propagated through the α colony with negligible crack deviation at α_s/α_s lamellae low angle boundaries. As discussed earlier, this was facilitated by the long slip length in the colony microstructure in the cast alloy. Cracks were found up to 60 μm in length in the cast alloy, whilst cracks were found to be much shorter (approximately 10 μm) in the forged alloy, see Figure 8d. These findings in conjunction with the tensile results for the cast and forged materials, Figures 3 and 4, would suggest that the majority of ductility lost in the centrifugally cast Ti-834 alloy is strongly related to bulk microstructure and not entirely dependent on α -case formation at the surface.

As described in Section 2, the α -case was removed prior to testing from a number of the exposed tensile specimens in order to understand the exact contribution of the α -case on reduced ductility. As shown in Figure 9, a proportion of the ductility lost in the cast material due to exposure for 500 hours is recovered when the α -case layer is removed prior to testing. The tensile test results showed a ductility of 5.4% at 100h, 4.7% at 200h and 5.4% at 500h exposure times. It appears that α -case layer correlation with ductility is time dependent. For instance, the ductility was similar or slightly reduced after removing the α -case at 100h and 200h (from 6.2% to 5.4% at 100h, from 5.1% to 4.7% at 200h, respectively). However, the ductility increased from 1.8% to 5.4% after removing the α -case from the specimen exposed for 500 h at 500°C. It is evident that the α -case contributed a 3.6% ductility increment at maximum exposure time in this study. It appears that the brittle nature of α -case can cause deteriorating effects on fatigue property at its early stage formation as reported in [5]. However, comparing the tensile results from current study with the fatigue results in earlier investigations suggest that the α -case effect on failure mechanism is significantly different between the tensile and fatigue tests.

3.4 The Effect of Ti₃Al (α_2) Precipitates on Ductility in Ti-834 Alloy

Ti₃Al, *i.e.*, α_2 , precipitate has a DO₁₉ structure and is an ordered intermetallic form of the α phase. In general, α_2 precipitates enhances titanium alloy's strength and creep resistance via precipitation hardening mechanism. However, as any other intermetallic phases, α_2 is brittle and can cause reduction in ductility. It is reported that mobile dislocations are able to shear α_2 precipitates during tensile deformation; leading to a reduction in the local resolved shear stress on active slip planes [27]. However dislocation mobility is retarded on other (not activated) planes leading to planar slip and cause dislocation pile ups against grain boundaries in titanium alloys [28]. Thus, it is generally believed that α_2 phase is anisotropic, prone to localisation of slip and poor ductility [27] [28]. Therefore, the maximum amount of aluminium is limited in order to restrict the exceeded proportion of the DO₁₉ phase, which can result in low ductility and toughness if present above a critical volume fraction. Originally, Ti-834 and Ti-6242S were designed to limit α_2 formation by restricting Al to ~ 6% and supplementing this aluminium with tin and zirconium to achieve greater overall strength without loss of toughness through excessive DO₁₉ (α_2) formation.

Experimentally, dissolving the precipitates into the solid solution is an effective way to fully understand the effects of α_2 precipitates and silicides on mechanical properties. The silicide and α_2 precipitates solvus temperatures were calculated using JMatPro programme. As shown in Figure 10, the solvus temperature of α_2 phase and silicide in Ti-834 were determined to be 675°C and 1050°C, respectively. These solvus temperature were slightly different from the findings in [11], however, this is probably related to exact chemical composition variants for Ti-834 alloy used in their calculations. As described in Section 2, further heat treatments were conducted on exposed alloys at 800°C and 1000°C in order to dissolve any α_2 precipitates and silicides present in the material. First, in order to determine the effect α_2 precipitation on the ductility of centrifugally cast Ti-834,

previously exposed (500°C/500h) tensile specimens were subjected to a heat treatment at 800°C for 2 hours to dissolve the α_2 precipitates. It should be emphasised here, that the 800°C heat treatment temperature was selected aiming to dissolve all α_2 that existed in the alloy. Figures 11a and 11b show high-resolution JOEL 7800 SEM images of α_2 precipitates distribution in the centrifugally cast Ti-834 alloy exposed at 500°C/500h prior and subsequent to 800°C/2h heat treatment, respectively. As shown in Figure 11a, following the initial exposure the α lamellae was densely populated by α_2 precipitates with a range of 10-80 nm sizes in diameter. The image in Figure 11b shows that the vast majority of the α_2 precipitates were dissolved following 800°C/2h heat treatment. However there are still some precipitates up to 40nm in diameter present, see the same figure. The observed α_2 precipitates after the 800°C/2h heat treatment are likely to have precipitated during cooling from the annealing temperature. As predicted from the phase diagram in Figure 10, it is expected that all of the pre-existing α_2 precipitates dissolve during this heat cycle where the temperature was well above the α_2 solvus temperature. Moreover, the observed particles after the heat treatment have different (smaller) measured sizes and distribution, which suggests new α_2 particles were formed during cooling, see Figure 11b.

Figure 12 shows the tensile results for the centrifugally cast Ti-834 alloy after the heat treatments. It is clear from Figure 12 that α_2 precipitation coarsening effects on the ductility of the centrifugally cast Ti-834 after 500°C/500h exposure is not significant. These results contrast significantly with the work in [27] on Ti-60, [29] on Ti-834 and [10] on Ti-1100, Ti-6242S and Ti-834 where significant portions of lost ductility in lamellar structures was attributed to the presence of α_2 precipitates. The tensile ductility following 800°C/2h heat treatment was found to be almost identical (5.5%) to the prior results obtained at 500°C/500h with α -case removed (5.4% strain), see Figure 9. This aspect was further investigated through heat treating the originally 500°C/500h exposed specimen at 1000°C/2h. As shown in Figure 11c the alloy contains not only a higher concentration of α_2 precipitates than those found in the originally exposed material, but they are

generally coarser with diameters of up to 100nm. This also suggests that although the α_2 re-precipitated in bigger sizes during cooling, they did not effect, *i.e.*, reduce the tensile ductility, see Figures 11c and 12. On the other hand, the forged material which retained its ductility after 500°C/500h exposure was found to have a high concentration of α_2 precipitates with much finer sizes than those found in the centrifugally cast Ti-834 alloy; with diameters of 10-20 nm, see Figure 11d. It appeared that the homogenous distribution of the very fine α_2 precipitates and their high coherency with the α phase matrix may have assisted in alloy strengthening of the Ti-834 forged alloy with no reduction in alloy's ductility. It is difficult to ascertain the effect of heat treatment at 800°C/2h on the reduced ductility of the centrifugally cast material. Previous studies [2][10] have stated that the precipitation of α_2 particles significantly reduces the ductility of the Ti-834 alloy after long term exposure at similar working temperatures to this work. However, from the current heat treatment and following microstructure characterisation and tensile results, shown in Figure 12 it appears that dissolving the existed and coarsened α_2 precipitates during high temperature exposure and homogenous re-precipitate α_2 in much smaller sizes could only recover $\sim 0.2\%$ of the lost ductility during high temperature exposure.

3.5 The Effect of Silicides on Ductility in Ti-834 Alloy

It appeared that heating the cast material to 800°C in order to dissolve the α_2 precipitates had no significant effect on tensile ductility. However as shown in Figure 12, the majority of the lost ductility was recovered when specimens were heat treated at 1000°C/2h to dissolve silicides. These results indicate that the presence of silicides has a vital contribution in the ductility regression in the centrifugally cast Ti-834 alloy. Figure 13a and 13d show high-resolution backscatter SEM images for centrifugally cast Ti-834 prior and after 500°C/500h exposure, respectively. The 2D EDS silicon and zirconium maps for Figure 13a are shown in 13b and 13c and for Figure 13d in 13e and 13f, respectively. As shown in Figure 13a, small size silicides (~ 400 -900 nm in diameter) with irregular

shapes are located on the α/β phase boundaries throughout the cast material prior to any exposure. Figure 13d-f, show the concentration of silicides was increased in the centrifugally cast alloy after 500°C/500h exposure. The silicides were also found to be much coarser than those seen in the unexposed material; up to 2.3 μm in diameter. Furthermore, the exposure at 500°C for 500h caused the existing silicides to coarsen on α/β phase boundaries. It is evident from Figure 13g, that the silicide coarsening on α/β phase boundaries caused large voids formation around the precipitates. This is an indication that the silicide lost its coherency with the α matrix at this stage.

It is reported that silicon and zirconium present in near α alloys combine with titanium to form silicides of varying compositions [30] [31]. Singh, *et al.*, [31] identified silicide phase composition that formed at high temperature in near α titanium alloy, and they established that even with small quantities of β stabilising elements only silicides with a composition of $(\text{TiZr})_6\text{Si}_3$ were precipitated. The composition of the silicides found in this work was investigated using EDS analysis. Further analytical methods were used in this study to identify the precipitates, as all the EDS element peak intensities contained minor quantities of Al. This is expected from SEM-EDS data, and it suggests that not only the silicides but also the spectrums from surrounding matrix were collected even at high-resolution data collection. Here, in order to determine the correct silicide composition, titanium, zirconium, silicon and tin contents were plotted against aluminium wt% quantity. The results were then extrapolated to find zero values for aluminium and reveal the corresponding content of titanium, zirconium, silicon and tin correctly. In order to avoid unreliable EDS data acquisition a Monte Carlo simulation was performed using free online tool CASINO V3.3 software and it appears that the interaction volume for X-ray generation is $\sim 150 - 200 \text{ nm}$ in Ti-834 alloy using 8 kV acceleration voltage. Thus, only large silicide precipitates ($> 0.5 \mu\text{m}$) were selected for the chemical analysis in an attempt to keep the interaction volume ($150 - 200 \text{ nm}$) within the silicide itself. Furthermore, in order to obtain a reliable data 12 silicide point data were analysed and averaged to obtain exact chemical composition.

Figure 14 shows backscatter SEM images and EDS 2D maps for forged Ti-834 alloy prior (Figure 14a-c) and post 500°C/500h exposure (Figure 14d-e). As shown in Figure 14a, silicides were also found in the forged material prior to exposure. However, silicides were only present in the transformed β area, *i.e.*, on the α_s/β boundaries, and not within equiaxed α_p areas, see the same figure. It was evident that the early silicide precipitation occurred on the β phase in both forged and cast Ti-834 samples, see Figures 13 and 14. The silicides in the forged material have a similar irregular shape to those found in the cast alloy; however some were much smaller in size; in the range of 80nm – 170nm, see Figure 14b-c. Some precipitates up to 200nm in diameter were also found on α_s/β phase boundaries. The fine silicide size in the wrought alloy may be attributed to the smaller volume fraction and width of β phase in between α lamellae in the bimodal microstructure of the forged material. Although attempts were made to chemically analyse the silicides found in the forged material, see Figure 14c, the silicides were too small for EDS analysis from 2D EDS maps. Figure 14d-e shows the microstructural and chemical analysis of the forged material after 500°C/500h exposure. It appears there is no significant increase in the overall concentration of silicides present in the duplex microstructure. This further explains the ductility preservation (17.8% strain) of the forged Ti-834 alloy after 500°C/500h exposure. It is also rather apparent that the existing silicides have not coarsened during the exposure; their diameters remained unchanged at approximately 140-200 nm. Therefore, in order to obtain a reliable chemical composition data for silicide in this study, the chemical analyses was fully dependent on the cast alloy as the silicide precipitates were much larger in size (up to 2.5 μm) than in the forged alloy. Figure 14f shows the average EDS chemical data collected from 12 large ($> 0.5 \mu\text{m}$) silicide precipitates from the cast sample. The relatively low wt% of detected Aluminium shows that the point investigation was successful in isolating the silicide chemistry, although some Aluminium counts were inevitable from stray X-Rays from the rest of the sample. In contrast to the previous work in [30] [31] a silicide composition of $\text{SiTi}_{1.5}\text{Zr}$ or $\text{Ti}_3(\text{ZrSi})_2$ was identified by the EDS results in this study. This

composition was similar to JMatPro phase prediction shown in Figure 10.

Figure 15a-c shows the microstructure (a) and EDS chemical analyses (b and c) of centrifugally cast Ti-834 alloy following 500°C/500h exposure and heat treatment at 800°C/2h. It is clear from the figure that 800°C/2h heat treatment has enabled further silicide precipitation and coarsening of the existing silicides to occur. As shown in Figure 15d, further voids were formed on silicide/matrix boundaries after 800°C/2h annealing. An area in Figure 15d was further magnified and showed in 15h; it shows that the early silicide precipitation occurred on the β phase. It appears that further silicide precipitation; coarsening and debonding during 800°C/2h annealing has greater effect on the ductility and overcome most of the recovery that might have occurred from dissolving the α_2 precipitates. Figure 15e-g shows the microstructure and chemical analyses of centrifugally cast Ti-834 alloy following 500°C/500h exposure and 1000°C/2h heat treatment. As shown in the figures the vast majority of the widmanstatten colony microstructure was free from silicides. It is apparent that the 1000°C heat treatment intended to dissolve all of the silicides had a dramatic effect on the tensile ductility of the centrifugally cast alloy; with 80% of the lost ductility recovered, see tensile results in Figure 12. Further analysis of the microstructure; see Figure 15e-g, showed that there were however isolated regions that still contained some silicides after the 1000°C/2h heat treatment. This may be correlated to the heterogeneous distribution of the alloying element, where some areas have nominally higher silicon content than other areas. This occurs due to the high partitioning coefficient silicon has in titanium, which allows it to partition to the last areas to freeze on cooling. Furthermore, the silicide solvus temperature calculated using JMATPro is 1050°C, see Figure 10, 50° above the heat treatment temperature used here. Therefore, a small volume fraction of silicide is expected after 1000°C/2h annealing.

The absence of silicides in α_p as shown in Figure 14 was one of the focus point in the current study. Further high resolution imaging and EDS analysis were conducted in this study in order to

understand the silicide segregation in the transformed β area, and in particular on α_s/β boundary. The alloying element partitioning can clearly be seen in Figure 16. Using high resolution imaging a location of a 250 nm width β phase (Figure 16a) was selected as reference for all the EDS element intensity profile position in the same figure. It is clear from Figure 16b that Ti showed very low intensity in the centre of the β phase with a width of 110 nm line profile. Whereas, Al showed the lowest intensity within β and the adjacent α_s lamellae, covering 580 nm width of lowest intensity, Figure 16c. This is accompanied with significant partitioning of molybdenum into the β phase with exact width as β , Figure 16f. Whilst, Zr and Si have the highest concentration within the silicide particles, shown in Figure 16d and 16e, respectively. However, a high intensity Zr in a width of 630nm was found in β and adjacent α_s . In order to verify this 2D EDS results, line EDS scans were performed using a minimum SEM beam diameter (spot size of 5nm) to reduce electron interaction volume and obtain high resolution and accurate EDS point data. Figure 17 shows Al, Mo, Ti and Nb EDS element line scan profiles for a selected area in the cast alloy. It is clear from Figure 17a, silicide particles formed on the α_s/β boundary, separated from α matrix and large voids were formed around them. A magnified area is shown in Figure 17b where the EDS line scans were performed. It is clear from the Al line profile that the partitioning creates an aluminium-depleted zone extending to approximately 2.5 μ m in the both sides of the β laths, see Figure 17a-b. Al concentration was reduced from 5.5 wt% in the centre of α_s to ~2 wt% in β phase centre. The same trend was found for Ti, but to a less extent, where 84 wt% in α_s centre reduced to ~ 72 wt% in β centre. In contrast molybdenum and niobium peak intensities were found to be highest in the centre of β phase centre; 9.5 and 4.5 wt% respectively. It should be noted no partitioning or intensity change was observed for Sn (6 wt% \pm 0.5) in the line scans conducted for the same area in Figure 17b.

The alloying element partitioning was further investigated in the forged alloy in order to study the microstructure effect on partitioning mechanism. Figure 18 show EBSD maps and EDS analysis of Ti-834 alloy after 500°C/500h exposure. It is clear from Figure 18a-d, that highest Al concentration

was found in α_p and lowest in the β transformed matrix, *i.e.*, α_s lamellae structure. In contrast, Zr highest intensity was found in α_s lamellae region and lowest within the α_p equiaxed grain. The high magnified transformed β area in Figure 18e-f, showed that basket-weave morphology was present in some area of the β -transformed region in between α_p grains. Further EDS 2D maps and line scans were performed on the α_p and β -transformed boundary, see Figure 18g-h. From the figure, the high Al and low Zr intensities in α_p is further demonstrated. It is also evident from the EBSD derived IPF map in Figure 18f, that the lamellae in the β -transformed area possessed different orientations, separated by high angle grain boundary and forming basket-weave morphology structure. As stated earlier this basket-weave morphology can provide superior crack propagation resistance compared to the lamellae colony microstructure present in the cast alloy, which show low misorientation angles between the aligned lamellae, see Figure 5. This attributed to further strengthening and increased plasticity of the forged Ti-834 alloy.

3.6 Element Partitioning Effects on Silicide Formation, Coarsening and its Composition

All the collected 2-D EDS maps and line scans data are illustrated schematically in Figure 19. It is evidence that considerable amount of element partitioning was occurred during Ti-834 alloy solution heat treatment and aging. Further partitioning occurred during exposure at 500°C/500h, which enhanced silicide/matrix debonding and particles coarsening. It is clear from the figure that Al and Ti partitioned in α_p , resulting in high concentrations in α_p and low concentrations in α_s lamellae. These results are also in agreement with Salem, *et al*, findings [32]. However, in this study Al and Ti displayed even lower concentrations and created Al depleted zones in the vicinity of α_s and the lowest level for both elements within β phase.

It is well established in literature that the α_s lamellae are softer than equiaxed α_p grains as a consequence of the alloy element partitioning effects [32], [33]. The Al partitioning makes α_p

stronger, and α_s weaker. Moreover, the Al depletion and nano-scale partitioning observed in the α_s/β boundaries resulted in easy crack initiation and promotes propagation in the centrifugally cast colony microstructure as demonstrated in Figure 6a-c. However, it appears that the Al and Ti partitioning in the forged alloy could not reduce the ductility of the alloy due to the exhibition of duplex microstructure with basket-weave morphology of α_s in some areas of the β -transformed region. It is reported that an increase to 5.2 atomic % of Al almost doubles the τ_{crss} or yield strength for basal slip [32-37]. Therefore the Al depletion level from 5.5 in the α_s centre to 1.8 wt% in the β phase center, shown in Figures 16 and 17 have theoretically reduced the basal slip τ_{crss} by nearly half. It should be also noted that in the current study the tensile tests were conducted at RT (20°C); where basal slip activation is even easier than at high temperature [1] and in α_s than in α_p [20]. This facilitated easy basal slip activation in the α_s as it is predicted by the EBSD derived Schmid factor maps in Figure 6.

As shown in Figure 17 and illustrated in Figure 19a, molybdenum and niobium were partitioned in the β phase with 10 and 4 wt%, respectively and zero wt% concentration in α_s centre. This is expected, as Mo is strong β stabiliser and the solid solubility of Mo in the α phase is very low (1%) compared to V (3%) [1], [7], [11]. Mo is used in preference to V in creep resistant Ti alloys, in order to improve both creep resistance and oxidation resistance. In Ti-834, compared with Ti-6242S, Mo was partly replaced with Nb, for a further improvement to oxidation resistance. It is clear from Figures 16 and 19 that Si has very low concentration in both α and β phases. This is also expected as Si has limited solubility in Ti, and is added to Ti-834 to improve creep resistance, however it is maintained between 0.25 to 0.35 wt% in the alloy to avoid excessive brittle silicide formation. Although it is generally believed that Zr behaves neutrally as it has complete solubility in α and β phases in Ti, however, it has high concentration on α_s/β phase boundary (4.5 wt% and α_s/β boundary and 2 wt% within α_s), see Figures 16 and 19b. This facilitated an easy diffusion of Zr from high Zr zones to silicide particles and causes coarsening and further formation of new

particles. The high affinity of Zr to Si allowed the highest concentration of Si and Zr with the lowest concentration of Ti on α_s/β boundaries to form hard $Ti_3(SiZr)_2$ precipitates. This is also in agreement with phase predictions in Figure 10. The partitioning of Ti, Si and Zr facilitated a thermodynamically preferred condition to form $Ti_3(SiZr)_2$ in transformed β , *i.e.*, α_s region but not in α_p regions. This is caused the centrifugally cast Ti-834 with a fully colony microstructure to have a higher volume fraction of silicides than in the forged alloy, *i.e.*, duplex microstructure, where it has 36% of α_p silicide free region. Thus, the volume fraction of α_p can play a vital role in strengthening and increasing ductility of the alloy. From the current study, a high volume fraction ($\sim 35\%$) with small size of equiaxed α_p ($\sim 20 \mu m$) in duplex microstructure provided an optimum strength and ductility for Ti-834 at both RT and HT exposures. It also appears that the basket-weave morphology in some areas of the β -transformed region in forged duplex alloy allowed less silicide coarsening. This may be due to different partitioning level between fully colony and basket-weave morphology.

It is evident that the alloying element partitioning is strongly microstructure dependant. In the forged alloy, the silicide particles were small in size, coherent and homogenously distributed in the duplex microstructure, in particular in β -transformed areas, see Figure 14. The precipitated and slightly coarsened silicide particles were remained relatively coherent during $500^\circ C/500h$ exposure and unlike in colony microstructure, the surrounding voids were not formed. It seems that the high volume fraction of α_p in the forged alloy, played a vital role in this relatively uniform partitioning across the bulk materials. On other hand, in the absence of α_p , as in the cast colony microstructure, the element partitioning during heat treatment and aging allowed much higher Al content in the centre of the lamellae and stronger partitioning of Zr, Si, Mo and Nb into or in the vicinity of β phase. This caused the silicide coarsening and debonding from the matrix during $500^\circ C/500h$ exposure in the cast alloy. It should be emphasized here that in this near α alloy, the amount of β phase is limited and it is appeared that minimum amount of partitioning was occurred where there was no β phase and low misorientation angles ($> 1^\circ$) in between lamellae. Furthermore, a

maximum amount of partitioning in the cast alloy occurred in the very large width lamellae areas (indicated by red dashed circles in Figure 2). It seems that these areas replaced α_p in enhancing the partitioning effect. However as can be seen from the same figure they are not homogeneously distributed across the microstructure and thus caused further silicide heterogenous distribution in the cast alloy.

In summary, to the authors' best knowledge this is a first comprehensive study to quantify the effects of each microstructural parameter individually on the ductility regression in the Ti-834 alloy. This type of microstructure parameters effects' quantification will assist greatly in optimising the mechanical properties of the alloy during processing. Furthermore, determining the parameters intercorrelations using this method will also assist in materials design, hence the chemical composition modification of the alloy. Figure 20 summarises the results in the current study and illustrates the comparison between strain/stress data for as-received forged and as-received centrifugally cast Ti-834 prior to heat exposure. A total of 16.7% ductility regression observed in centrifugal cast microstructure can be quantified as follow. It is evident from the figure that the 7.1% strain differences between the cast and forged alloy are related to microstructural variations including; morphology, lath widths, grain size and shape, grain orientations, texture intensity and components as well as microtexture, Section 3.2. A total of 9.6 % strain loss in the centrifugally cast Ti-834 after aging at 500°C/500h can be quantified as; 3.6% due to α -case formation during high temperature exposure, Section 3.3; 0.2% due to α_2 -precipitates coarsening, Section 3.4; 4.4% due to further silicide formation and coarsening, Section 3.5; 1.4% due to further microstructure changes during high temperature exposure such as lath width, $\alpha_{lamellae}/\alpha_{lamellae}$ and $\alpha_{lamellae}/\beta$ grain boundary weakening though further void formation and alloying element segregation, further Al and Ti partitioning during again, MC carbide formation coarsening, overall texture alteration and easy $\langle c+a \rangle$ slip system activation at high temperature. It should be emphasised here, other

processing conditions and testing environments including O₂ content are not considered in this study.

4. Conclusions

In the current study the effect of high temperature exposure on the reduction in ductility of the Ti-834 alloy is investigated. The microstructure characterisation of two differently processed alloys, namely centrifugally cast and forged Ti-834 alloys, were carried out prior and following mechanical testing, heat treatment and various exposure time and temperatures. The conclusions from this study are bulleted below:

- It is shown that the forged alloy is stronger and more ductile than its cast equivalent in the unexposed condition; having significantly higher strength with both the UTS and 0.2% proof stress values being approximately 10% higher than those of the cast material. The wrought alloy is also more ductile recording a failure strain of 18.4% compared to 11.3% for the cast alloy. Exposure at 500°C for extended times does not affect the tensile ductility of the wrought form of Ti-834.
- Exposure at 500°C/500 h was found to develop a uniform layer of α -case between 5-7 μ m in depth in both forged and cast alloys.
- The EBSD studies suggest that α lamellae orientated favourably for basal $\langle a \rangle$ slip provided the easiest path for trans-lamellar crack propagation. In addition, lamellae unfavourably oriented for basal $\langle a \rangle$ slip and favourably oriented for prismatic $\langle a \rangle$ slip tended to deflect or arrest the crack.
- In the centrifugally cast Ti-834 alloy, which has a fully colony microstructure, the crack initiation occurred at a prior β grain triple junction, where three or more prior β grains with different crystallographic orientations meet.
- Exposure at 500°C for extended periods of time greatly affects the tensile ductility of the cast form of Ti-834. A reduction in ductility of approximately 84% is seen when the alloy is exposed

at 500°C for 500 hours if the α -case layer is retained. Intermediate losses in ductility are seen when the alloy is exposed for 100 and 200 h. Removing the α -case layer prior to the testing could recover 3.6% of the lost ductility. It appears that α -case formation has less pronounced effects on tensile ductility than its effects of fatigue crack initiation and propagation reported in the literature.

- It appears that α_2 precipitation does not have a significant effect on the tensile ductility of the cast alloy as only a recovery of $\sim 0.2\%$ of lost ductility is seen after heat-treating the alloy at 800°C.
- Fine incoherent silicides of composition $Ti_3(SiZr)_2$ are found at α_s/β phase boundaries in both the cast and wrought alloy before any exposure. The silicides found in the cast material being far coarser than those seen in the wrought alloy. Moreover, the existing silicides in the cast material coarsen and new silicides were formed and precipitated during exposure at 500°C/500h.
- The silicide solvus temperature of the cast alloy appears to be higher than 1000°C, this results in small regions retaining silicides after the 1000°C/2h heat treatment. Silicide precipitation and coarsening was responsible for a 4.4% ductility loss after prolonged exposure at 500°C/500h of the cast alloy.
- A model for silicide precipitation in fully colony and duplex microstructures was established. It was evident that Al and Ti depletion in the vicinity of the β phase in the fully lamellae structure, *i.e.*, α_s area, reduces the strength of the alloy and facilitates the formation of $Ti_3(SiZr)_2$ precipitates. Furthermore, the silicides were not formed in α_p (high Al, Ti and low Zr areas) in the forged duplex microstructure, which allowed better mechanical performance and ductility than that of the cast alloy, *i.e.* fully colony microstructure.
- A high volume fraction ($\sim 35\%$) with small size of α_p ($\sim 20 \mu m$) in duplex microstructure provides optimum strength and ductility for Ti-834 at RT and HT exposures.

5. Acknowledgments

The authors would like to thank EU CleanSky for the financial support under (GOTA) Greater Operating Temperature Alloy programme, Timet UK for supplying the Ti-834 material used in this project, Doncaster Settas/UK for producing the centrifugal cast alloys and Forgital Italy S. P. A./Italy for producing and supplying the forged alloys in the form of forged rings sections. Special thanks to Professor Nick Green at Birmingham University, Roger Thomas and Paul Garratt at Timet for the useful discussion throughout this project.

References:

- [1] G. Lutjering and J. C. Williams, Titanium, 2nd edition, Berlin: Springer, 2007.
- [2] C. E. Shamblen, “Embrittlement of Ti Alloys by Long Time, High Temperature Exposure” Metall. Trans., vol. 2, pp. 277–280, 1971.
- [3] R. Gaddam, B. Sefer, R. Pederson, and M.-L. Antti, “Study of alpha-case depth in Ti-6Al-2Sn-4Zr-2Mo and Ti-6Al-4V,” IOP Conf. Ser. Mater. Sci. Eng., vol. 48, 012002, 2013.
- [4] Z. Abdallah, K. Perkins, and S. Williams, “Alpha-case kinetics and surface crack growth in the high-temperature alloy Timetal 834 under creep conditions” Metall. Mater. Trans. A Phys. Metall. Mater. Sci., vol. 43, no. 12, pp. 4647–4654, 2012.
- [5] R. Gaddam, M. L. Antti, and R. Pederson, “Influence of alpha-case layer on the low cycle fatigue properties of Ti-6Al-2Sn-4Zr-2Mo alloy” Mater. Sci. Eng. A, vol. 599, pp. 51–56, 2014.
- [6] A. L. Pilchak, W. J. Porter, and R. John, “Room temperature fracture processes of a near- α titanium alloy following elevated temperature exposure” J. Mater. Sci., vol. 47, no. 20, pp. 7235–7253, 2012.
- [7] M. J. Donachie Jr, Titanium: A Technical Guide, 2nd Edition, Ohio, Materials Park 2000.
- [8] R. Gaddam, B. Sefer, R. Pederson, and M.-L. Antti, “Oxidation and alpha-case formation in Ti-6Al-2Sn-4Zr-2Mo alloy” Mater. Charact., vol. 99, pp. 166–174, 2015.

- [9] R. W. Evans, R. J. Hull, and B. Wilshire, "The effects of alpha-case formation on the creep fracture properties of the high-temperature titanium alloy IMI834" *J. Mater. Process. Technol.*, vol. 56, no. 1–4, pp. 492–501, 1996.
- [10] W. T. Donlan, J. E. Allison, and J. V. Lasecki, "The Influence of Thermal Exposure on Properties and Microstructure of Elevated Temperature Titanium alloys" *Titanium 92, Science and Technology*, Warrendale, Minerals, Metals & Materials Society, pp. 295–30, 1993.
- [11] G. Lütjering, "Influence of processing on microstructure and mechanical properties of ($\alpha+\beta$) titanium alloys" *Mater. Sci. Eng. A*, vol. 243, no. 1–2, pp. 32–45, 1998.
- [12] D.F. Neal, "Development of TIMETAL 834." *Materials Design Approaches and Experiences*, TMS Fall Meeting, Indianapolis, pp. 199–213, 2001
- [13] M. A. Daeubler, D. Helm, and G. Lutjering, "Influence of Heat Treatment on Microstructure and Mechanical Properties of Cast IMI 834" *Titanium 95, Science and Technology*, London, Institute of Materials, pp. 709–716, 1995.
- [14] C. Andres, A. Gysler, and G.Lutjering, "Correlation Between Microstructure and Creep Behavior of the High Temperature Ti Alloy IMI 834." *Titanium 92, Science and Technology*, Warrendale, Minerals, Metals & Materials Society, pp. 311-318, 1993
- [15] K. Prasad, R. Sarkar, P. Ghosal, D. V. V Satyanarayana, S. V. Kamat, and T. K. Nandy, "Tensile and creep properties of thermomechanically processed boron modified Timetal 834 titanium alloy" *Mater. Sci. Eng. A*, vol. 528, no. 22–23, pp. 6733–6741, 2011.
- [16] S. Dron, "Toward ACARE 2020: Innovative Engine Architectures to Achieve the Environmental Goals ," 26th Int. Congr. Aeronaut. Sci., Anchorage, Optimage Ltd,2008.
- [17] P. Lawrence, "Meeting the challenge of aviation emissions: an aircraft industry perspective" *Technol. Anal. Strateg. Manag.*, vol. 21, no. 1, pp. 79–92, 2009.
- [18] S. Wei and S. Lampman, "Centrifugal Casting" *ASM Handbook*, vol. 15: Casting, Warrendale, ASM International, pp. 667–673, 2008.

- [19] K. Prasad and S. V. Kamat “Effect of strain rate on tensile behaviour and fracture toughness of timetal 834 titanium alloy at ambient temperature, *Journal of Advanced Materials*, vol. 41, no. 1, pp. 64–73, 2009.
- [20] S. Biroasca, J. Y. Buffiere, M. Karadge, and M. Preuss, “3-D observations of short fatigue crack interaction with lamellar and duplex microstructures in a two-phase titanium alloy” *Acta Mater.*, vol. 59, no. 4, pp. 1510–1522, 2011.
- [21] S. Biroasca, J. Y. Buffiere, F. a. Garcia-Pastor, M. Karadge, L. Babout, and M. Preuss, “Three-dimensional characterization of fatigue cracks in Ti-6246 using X-ray tomography and electron backscatter diffraction” *Acta Mater.*, vol. 57, no. 19, pp. 5834–5847, 2009.
- [22] J. A. Hall, “Fatigue crack initiation in alpha-beta titanium alloys,” *Int. J. Fatigue*, vol. 19, no. 1, pp. 23–37, 1998.
- [23] M. T. Whittaker, W. J. Evans, R. Lancaster, W. Harrison, and P. S. Webster, “The effect of microstructure and texture on mechanical properties of Ti6-4,” *Int. J. Fatigue*, vol. 31, no. 11–12, pp. 2022–2030, 2009.
- [24] F. J. Humphreys and M. Hatherly, "Recrystallization and Related Annealing Phenomena" second Edition, 2004, ELSEVIER Ltd, Oxford, UK.
- [25] M. R. Bache, W. J. Evans, V. Randle, and R. J. Wilson, “Characterization of mechanical anisotropy in titanium alloys,” *Mater. Sci. Eng. A*, vol. 257, no. 1, pp. 139–144, 1998.
- [26] E. Uta, N. Gey, P. Bocher, M. Humbert, and J. Gilgert, “Texture heterogeneities in $\alpha\text{p}/\alpha\text{s}$ titanium forging analysed by EBSD-Relation to fatigue crack propagation” *J. Microsc.*, vol. 233, no. 3, pp. 451–459, 2009.
- [27] W. Jia, W. Zeng, J. Liu, Y. Zhou, and Q. Wang, “Influence of thermal exposure on the tensile properties and microstructures of Ti60 titanium alloy” *Mater. Sci. Eng. A*, vol. 530, no. 1, pp. 511–518, 2011.
- [28] A. Stroh, “Brittle fracture and yielding,” *Proc Roy Soc*, vol. 46, no. 223, pp. 404–14, 1954.

- [29] K. V. S. A. I. Srinadh, N. Singh, and V. Singh, "Role of Ti₃Al / silicides on tensile properties of Timetal 834 at various temperatures," *Bull. Mater. Sci.*, vol. 30, no. 6, pp. 595–600, 2007.
- [30] D. Neal and S. Fox, "The influence of silicon and silicides on the properties of near-alpha titanium alloys," *Titanium 92, Science and Technology*, Warendale, Minerals, Metals & Materials Society, pp. 287–295, 1993.
- [31] A. K. Singh and C. Ramachandra, "Characterization of silicides in high-temperature titanium alloys," *J. Mater. Sci.*, vol. 2, pp. 229–234, 1997.
- [32] A. A. Salem, M. G. Glavicic, and S. L. Semiatin, "A coupled EBSD/EDS method to determine the primary and secondary-alpha textures in titanium alloys with duplex microstructures" *Mater. Sci. Eng. A*, vol. 494, no. 1–2, pp. 350–359, 2008.
- [33] J. Suiter, "Deformation of a duplex titanium alloy," *J. Less Common Met.*, vol. 1, no. 6, pp. 476–479, 1959.
- [34] N. Wain, X. J. Hao, G. A. Ravi, X. Wu, "The influence of carbon on precipitation of Alpha in Ti-5Al-5Mo-5V-3Cr", *Mater. Sci. Eng. A* 527, pp. 7673-7683, 2010
- [35] C. L. Li, X. J. Mi, W. J. Ye, S. X. Hui, Y. Yu, W. Q. Wang, "Effect of solution temperature on microstructures and tensile properties of high strength Ti-6Cr-5Mo-5V-4Al alloy" *Mater. Sci. Eng. A* 578, pp.103-109, 2013
- [36] Z. X. Du, S. L. Xiao, Y. P. Shen, J. S. Liu, J. Liu, L. J. Xu, F. T. Kong, Y. Y. Chen, "Effect of hot rolling and heat treatment on microstructure and tensile properties of high strength Beta titanium alloy sheets" *Mater. Sci. Eng. A* 631, pp. 67-74, 2015
- [37] Y. Y. Chen, Z. X. Du, S. L. Xiao, L. J. Xu, J. Tian, "Effect of aging heat treatment on microstructure and tensile properties of a new Beta high strength titanium alloy" *J. Alloys Compd.* 586, pp. 588-592, 2014.

Figure Captions:

Figure 1: (a) The cylindrical tensile specimen geometry used in the current study, (b) the forged specimen coordinate axes with reference to EBSD scan area.

Figure 2: Optical micrographs showing the microstructure of Ti-834 as a) Centrifugally cast alloy in unexposed condition, b) wrought alloy in unexposed condition, c) Cast alloy post exposure at 500°C/500h, d) wrought alloy post exposure at 500°C/500h.

Figure 3: Stress-Strain curves showing the effect of exposure time on the tensile properties of Ti-834 centrifugally cast alloy.

Figure 4: Stress-Strain curves showing the effect of exposure time on the tensile properties of Ti-834 forged alloy.

Figure 5: EBSD orientation map of centrifugally cast Ti-834 alloy highlighting low misorientation angle between neighbouring lamellae (α_s) in colony microstructure.

Figure 6: 2D EBSD-IPF//LD maps from 3D-EBSD volume showing crack interaction with grain orientation at a) 50 μm , b) 100 μm and c) 200 μm below the surface, visualizing the crack initiation at prior β triple junction (3D crystal viewer superimposed on the maps). Five areas are indicated on the IPF maps by white dashed rectangular lines and are magnified individually. a1), b1) and c1) show EBSD-derived (0002) $\langle 11\text{-}20 \rangle$ and a2), b2) and c3) (10-11) $\langle 11\text{-}20 \rangle$ Schmid factor maps for the same area in (a, b and c).

Figure 7: EBSD-derived IPF//Y, Pole Figures, Inverse Pole Figures and ODFs for Cast (a) and (b) Forged alloys, (c) schematic representation of standard (0001) and (10-10) pole figures for ideal Basal and Transverse texture components.

Figure 8: Optical micrographs illustrating α -case formation after exposure at 500°C/500h on Ti-834 a) cast, b) forged alloy. The surface crack initiation and propagating through c) cast and d) wrought alloy are shown.

Figure 9: Stress-Strain curves showing the effect of α -case removal on the tensile ductility of exposed centrifugally cast Ti-834 alloy.

Figure 10: Simulated JMatPro phase diagram showing temperature versus wt% of the phases in Ti-834.

Figure 11: High-resolution SEM images showing α_2 precipitates in a) cast alloy after 500°C/500h exposure, b) after 800°C/2h and c) 1000°C/2h heat treatment, d) wrought alloy after 500°C/500h exposure.

Figure 12: Stress-Strain curves showing the effect of heat-treatment temperature on the tensile ductility of the exposed cast Ti-834 alloy.

Figure 13: High-resolution SEM images of centrifugally cast Ti-834, a) prior to, d) after 500°C/500h exposure. b) and c) show 2D EDS maps of silicon and zirconium, respectively for area in (a). e) and f) show 2D EDS maps of silicon and zirconium, respectively for area in (d). g) present void formation due to silicide coarsening on α_s/β phase boundary.

Figure 14: High-resolution SEM image of wrought alloy, a) and b) prior to exposure, d) after 500°C/500h exposure, c) chemical analysis of the area in (b), e) represent the chemical analysis for area (d), (f) show the composition of silicides observed in cast alloy.

Figure 15: High-resolution SEM image of 500°C/500h exposed centrifugally cast Ti-834, a) after 800°C/2h heat treatment, b) and c) show 2D EDS silicon and zirconium maps for area (a), d) show the brittle nature of coarsened silicide and void formation around it, e) after 1000°C/2h heat treatment, f) and g) 2D EDS silicon and zirconium maps for area in (e), h) shows silicide early stage formation on β phase.

Figure 16: Alloying element partitioning of (b) Ti, (c) Al, (d) Zr, (e) Si and (f) Mo in the vicinity of β phase shown in the SEM images in (a) for cast Ti-834 alloy.

Figure 17: Silicide formation on β and Al depleted zone in α_s shown in (a), the magnified area is shown in (b) where Al, Mo, Ti and Nb EDS lines scans are performed for cast Ti-834 alloy.

Figure 18: EBSD-derived band contrast (a) IPF//X (b) maps, EDS maps for Al (c) and Zr (d) for forged Ti-834 alloys after 500°C/500h exposure. EBSD-derived band contrast (e) IPF//X (f) maps,

the EDS 2D maps for high-magnified area of β -transformed area showing the basket-weave morphology, (h) Al and Zr EDS lines scan profiles for the purple and yellow lines indicated in (g).

Figure 19: Schematic illustration of the alloying element partitioning in Ti-834 following the exposure at 500°C/500h.

Figure 20: Quantification of the microstructural parameter effects on the tensile ductility of the centrifugally cast Ti-834 alloy. The stress-strain curves illustrate the as-received forged (blue curve) and centrifugally cast (red curve) Ti-834 prior to high temperature exposure.

Figure 1:

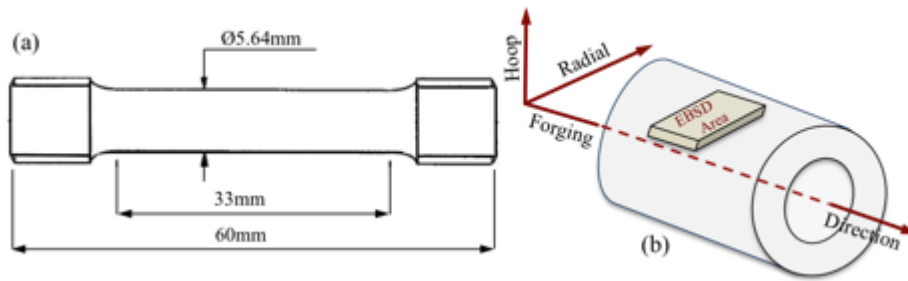


Figure 2:

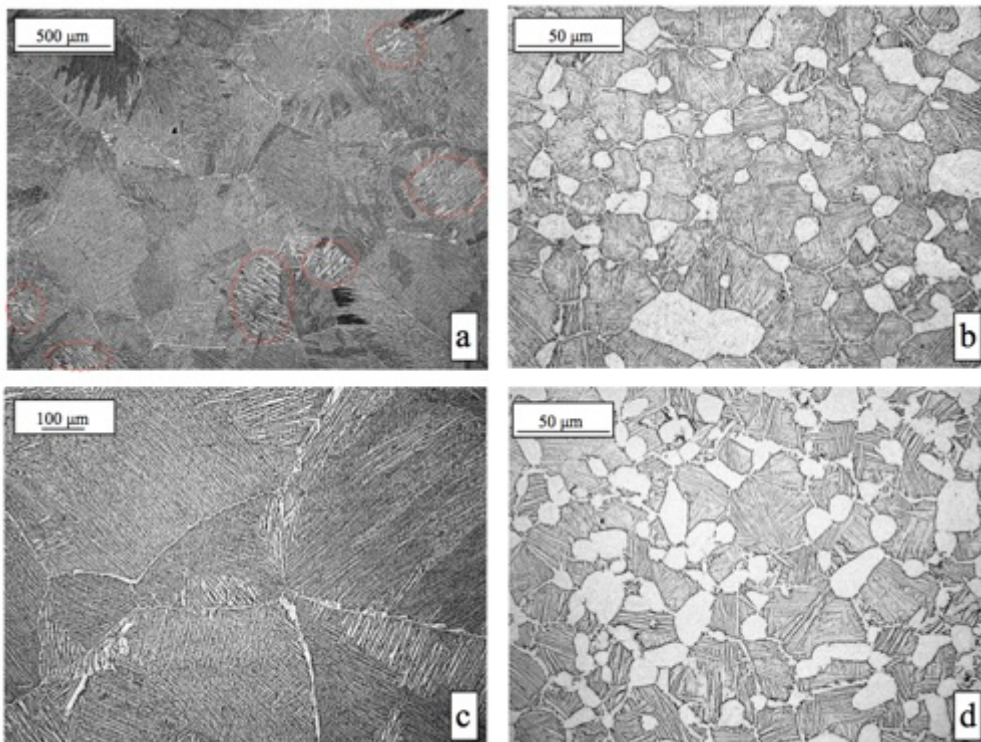


Figure 3:

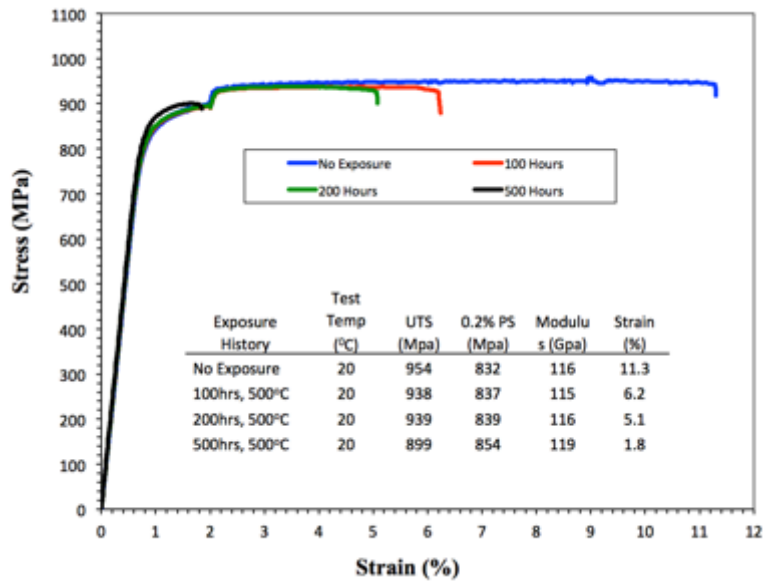


Figure 4:

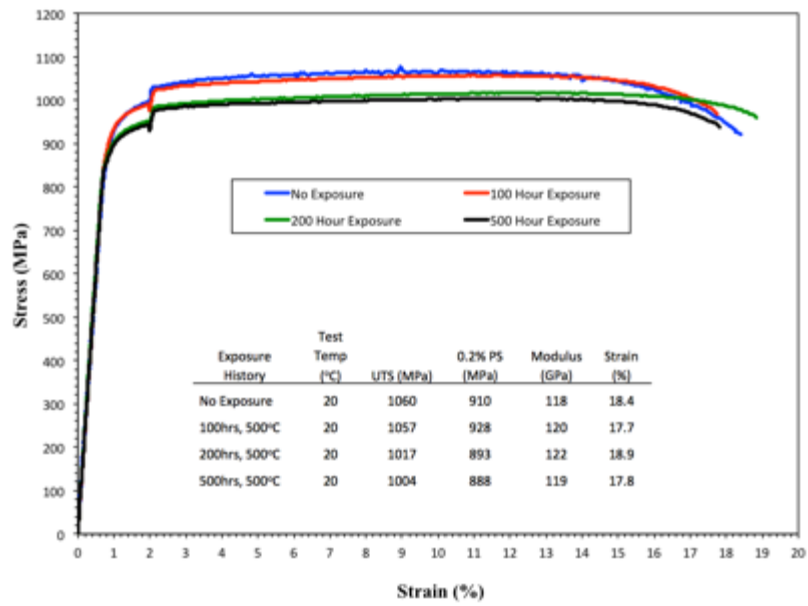


Figure 5:

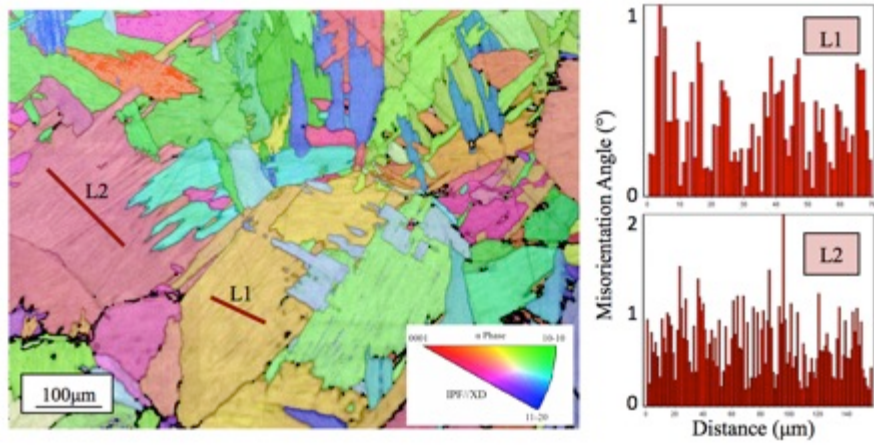


Figure 6:

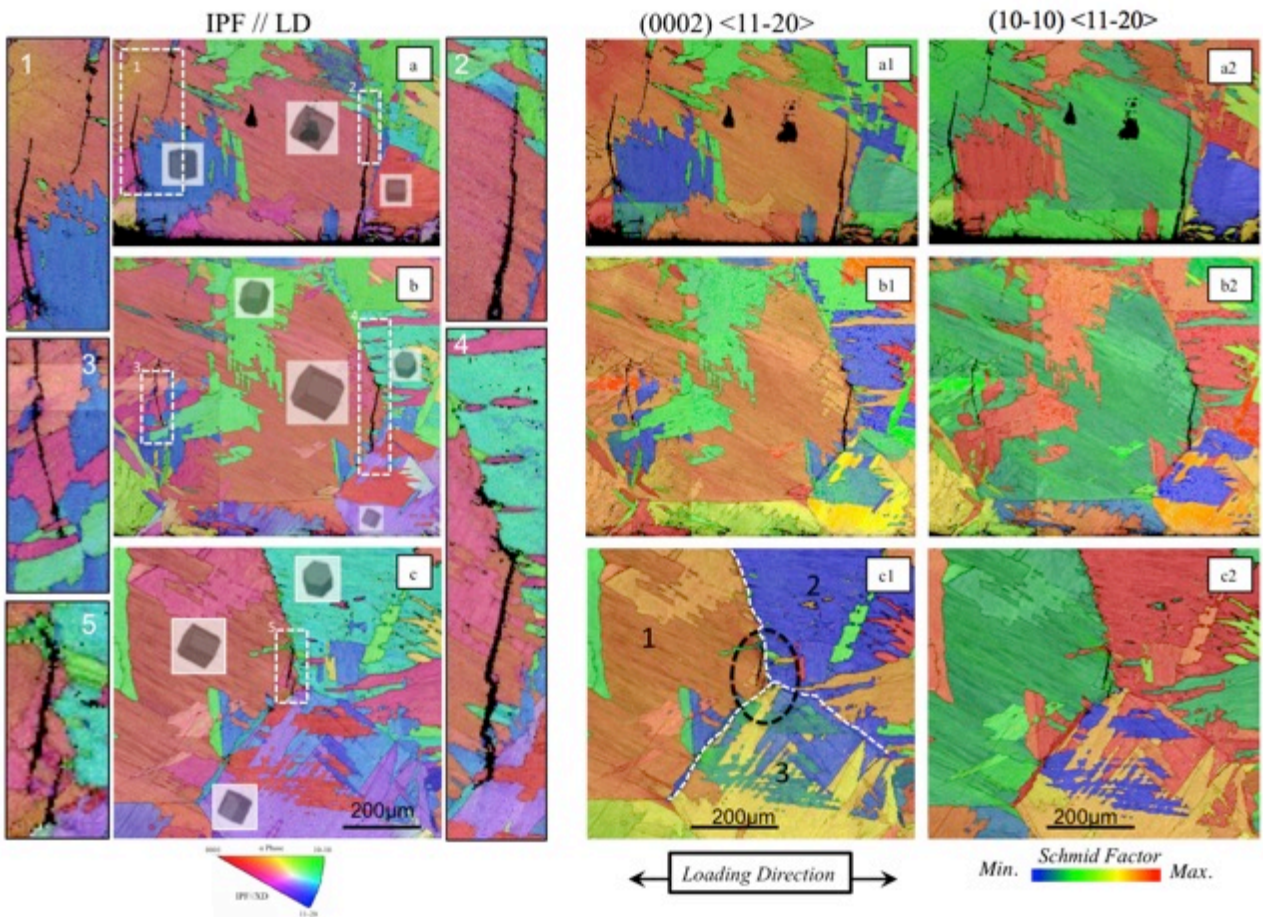


Figure 7:

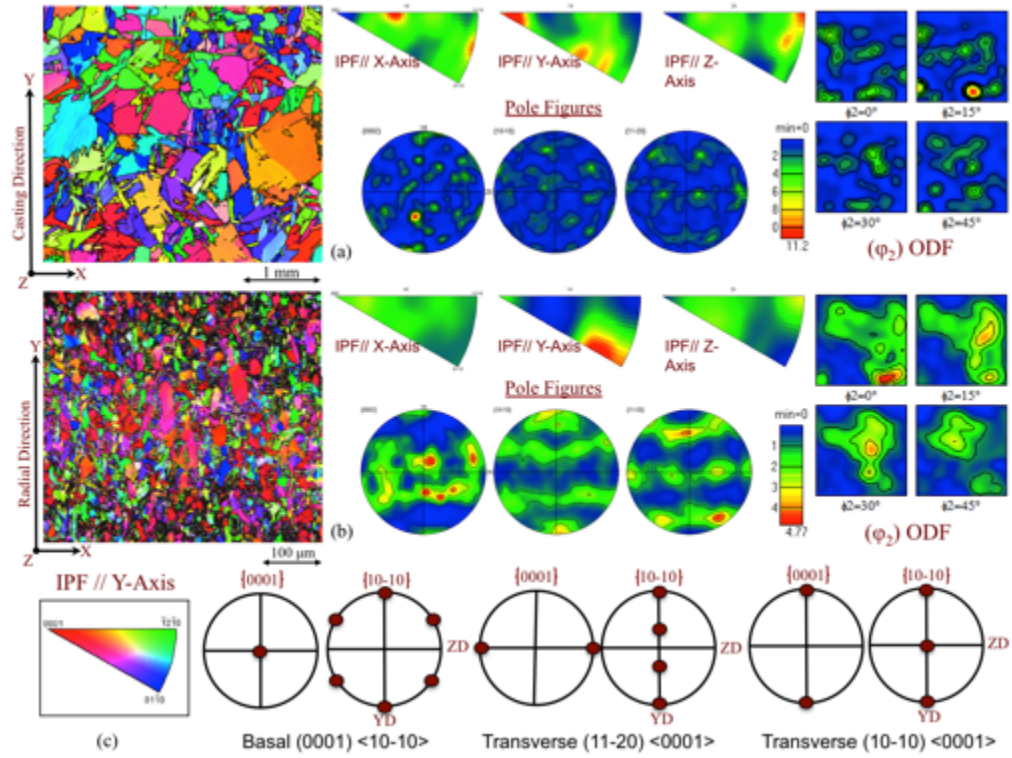


Figure 8:

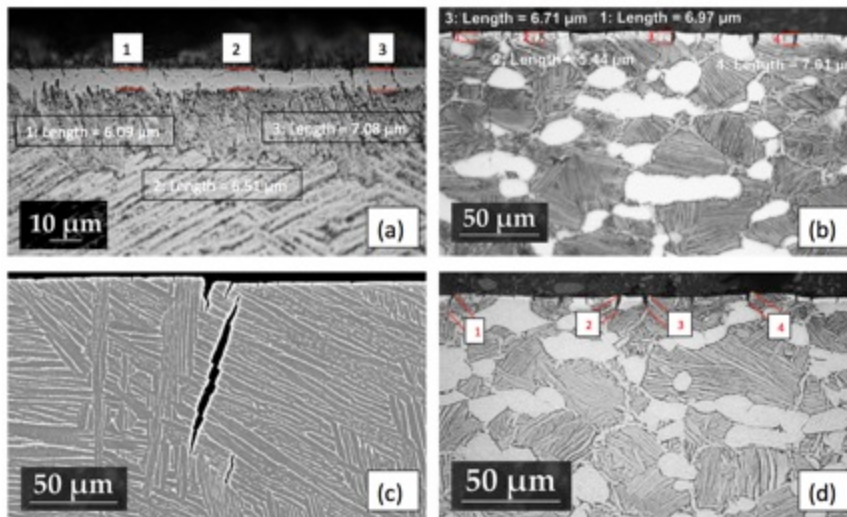


Figure 9:

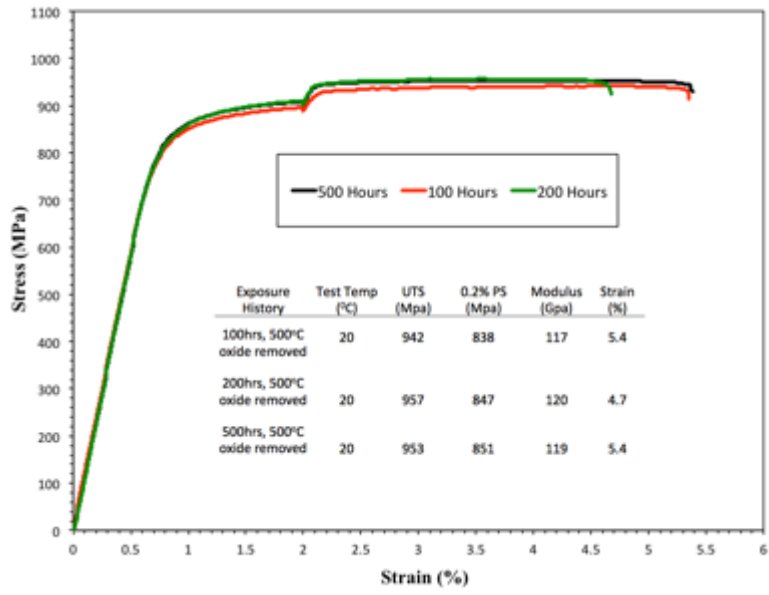


Figure 10:

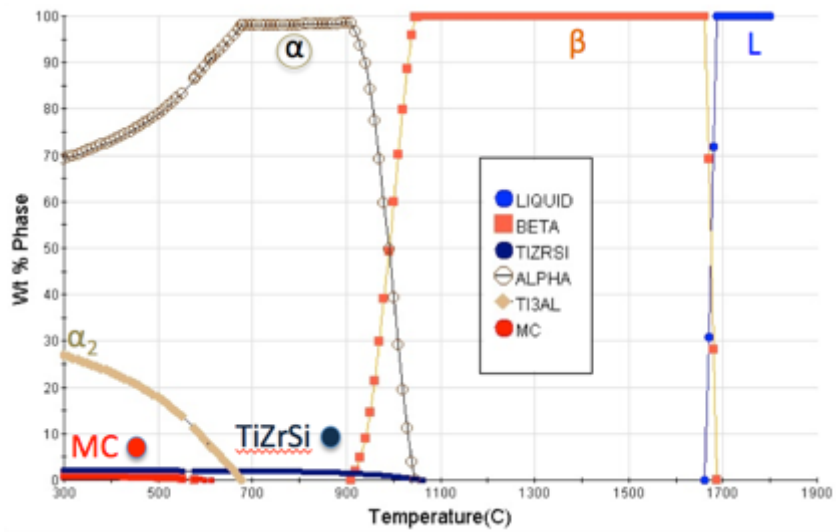


Figure 11:

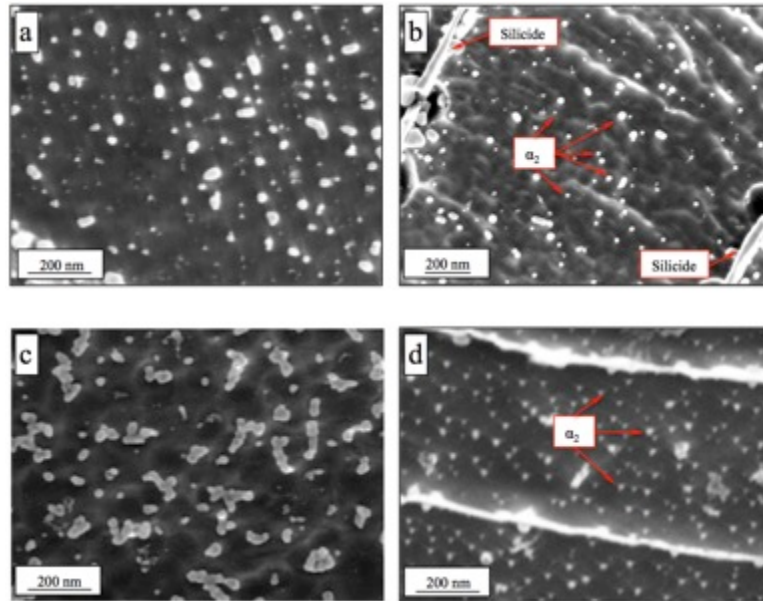


Figure 12:

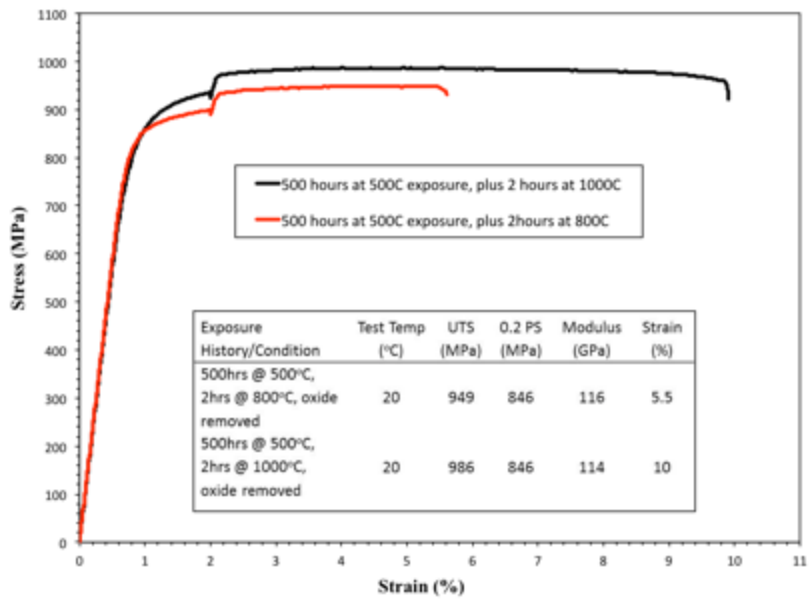


Figure 13:

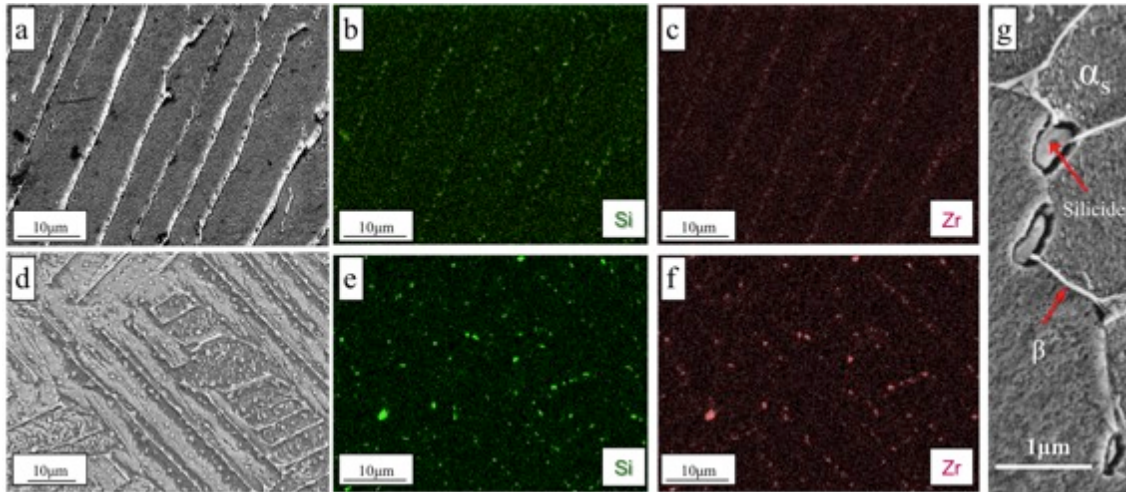


Figure 14:

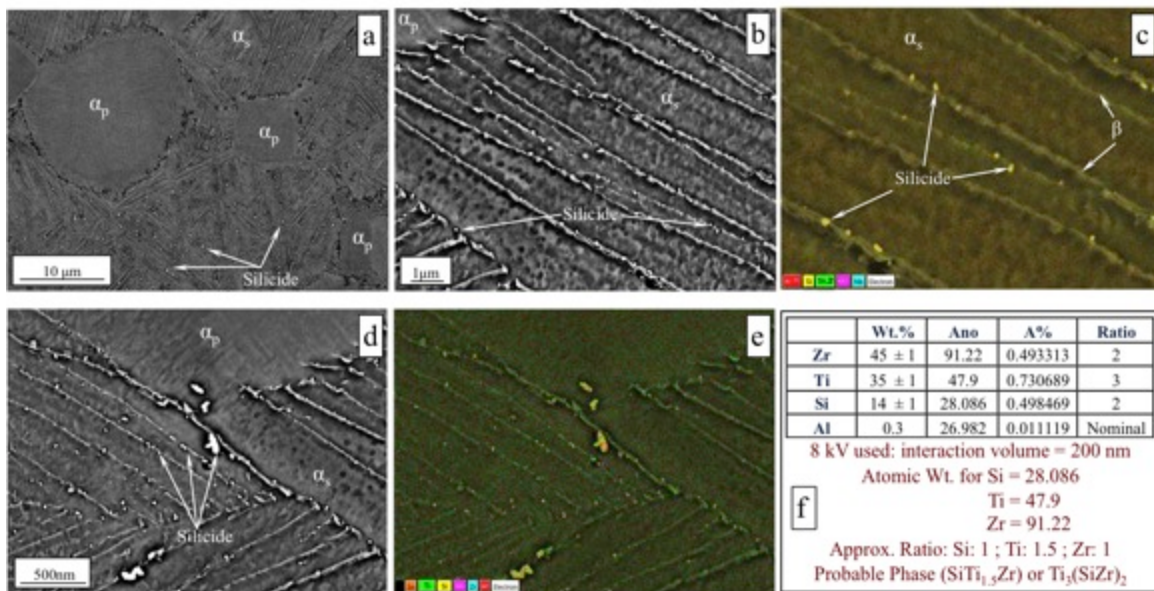


Figure 15:

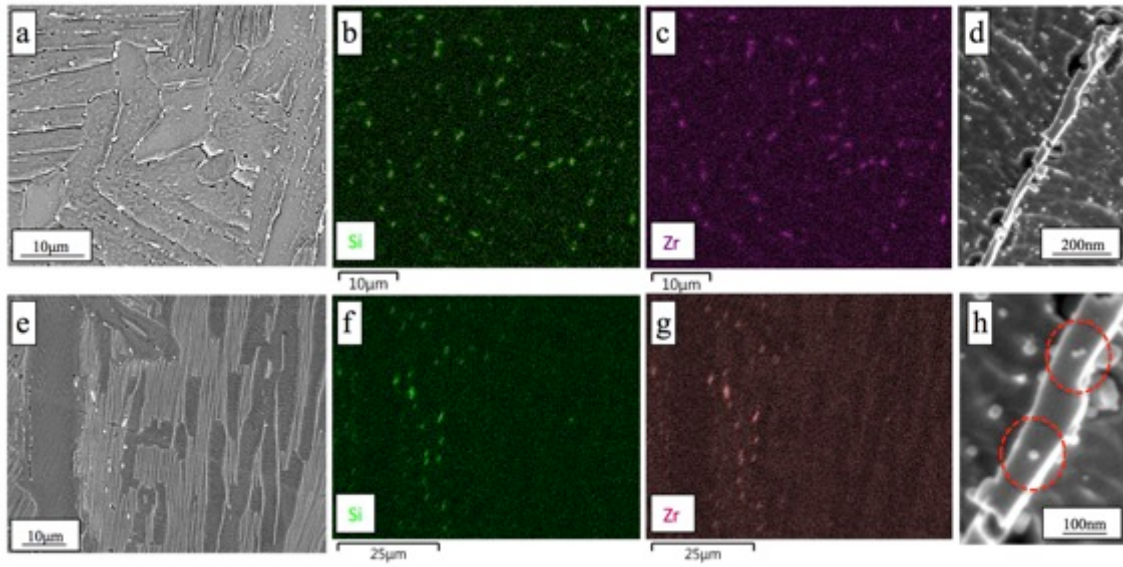


Figure 16:

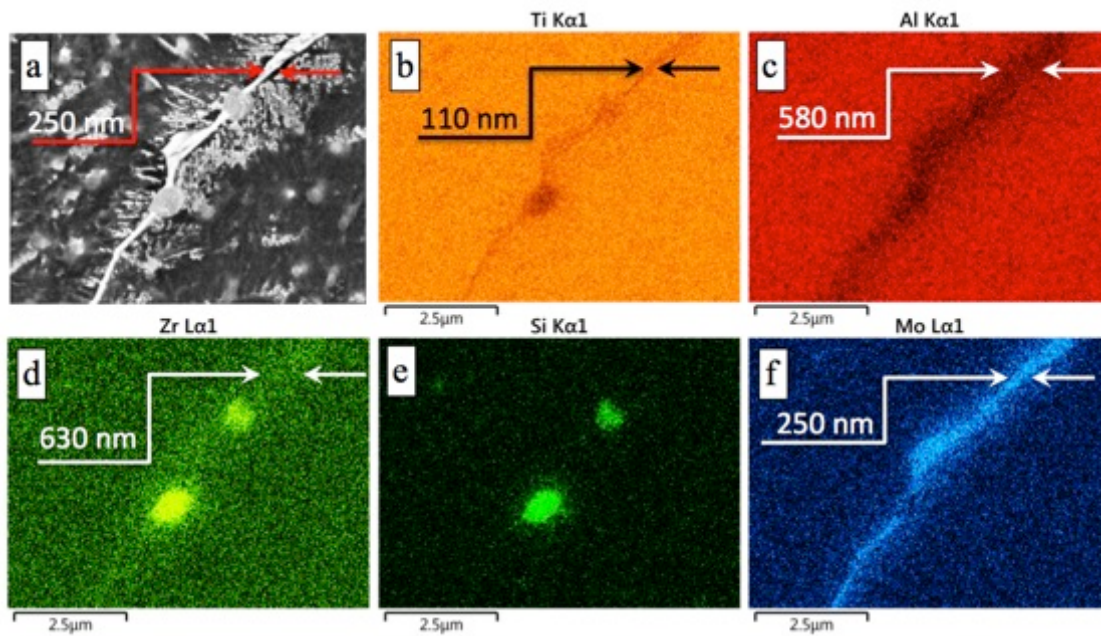


Figure 17:

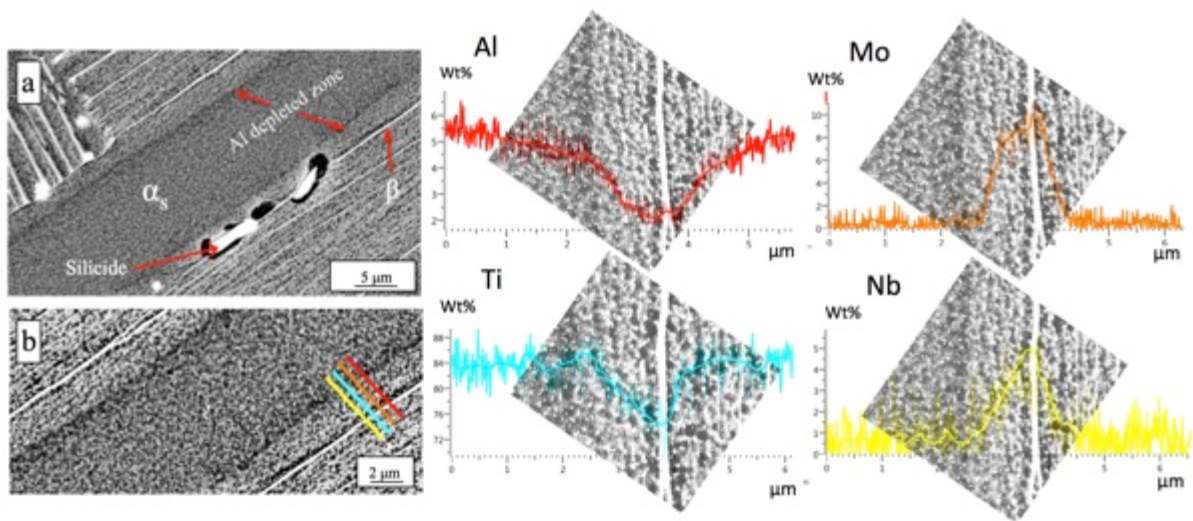


Figure 18:

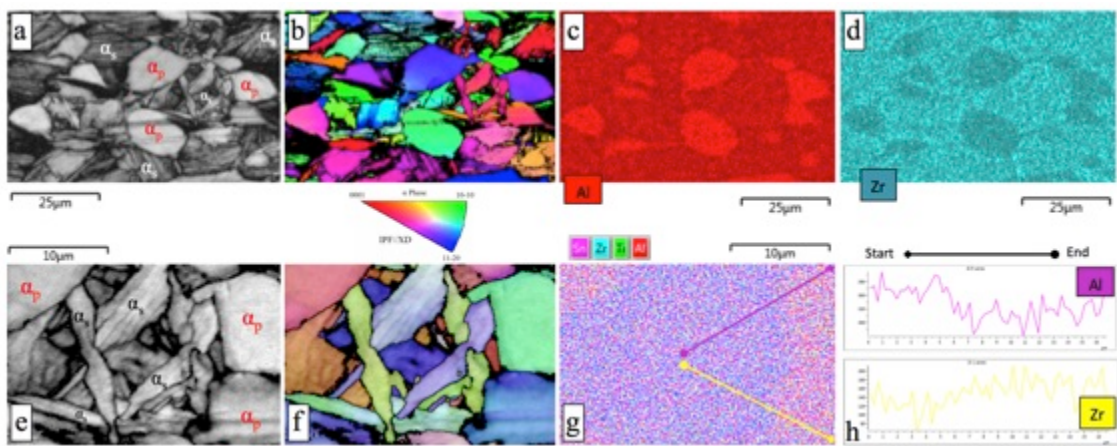


Figure 19:

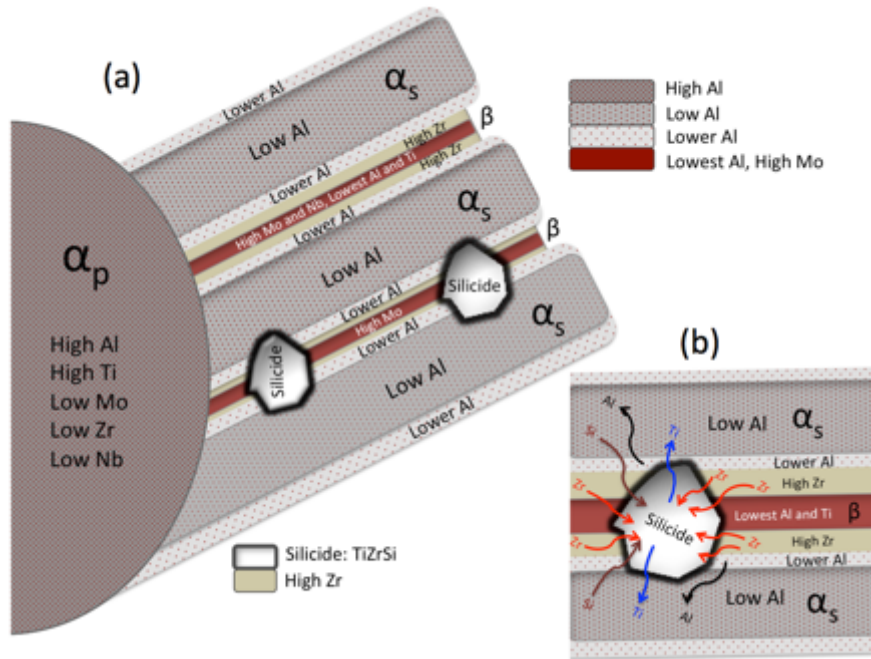


Figure 20:

